


3D-Structured Monoliths of Nanoporous Polymers by Additive Manufacturing

Sebastian Hock and Marcus Rose*

DOI: 10.1002/cite.201900149

 This is an open access article under the terms of the Creative Commons Attribution-NonCommercial-NoDerivs License, which permits use and distribution in any medium, provided the original work is properly cited, the use is non-commercial and no modifications or adaptations are made.

Recent advances in 3D printing provide great opportunities for the utilization of functional materials in chemical engineering and heterogeneous catalysis. In this work cylindrical monoliths with varying geometries of transport channels are designed and printed by a fused deposition modeling (FDM) 3D printer from thermoplastic polymers. Their hydrodynamic characteristics are investigated. For a proof of concept composite monoliths of microporous hyper-crosslinked polymers (HCP) are printed. They contain up to 40 wt % of HCP with an accessible specific surface area of up to $171 \text{ m}^2 \text{ g}^{-1}$.

Keywords: 3D printing, Hierarchical porosity, Hydrodynamic properties, Monolith, Porous polymer

Received: September 17, 2019; *revised:* December 05, 2019; *accepted:* February 05, 2020

1 Introduction

The morphology of a fixed bed or a structured packing in a reactor or column has a huge impact on flow-related properties such as mass transfer, fluid distribution, dispersion and pressure drop [1–3]. There have been many theoretical [1, 3, 4] and experimental [5] studies on various packing configurations, explicitly showing advantages in comparison to randomly packed beds. However, the practical implementation of optimally structured fixed beds in industrial applications has proven to be difficult [6–8].

The method of 3D printing with its versatility, high speed and low cost is exploited in many applications such as electrochemical devices [9], biomaterials [10], microfluid devices [11] and catalysis [12–15]. The most common additive fabrication methods in chemical engineering are extrusion techniques, stereo lithography, inkjet printing and powder-based systems [15]. Fused deposition modeling (FDM) is a printing process based on melt extrusion and deposition of various kinds of thermoplastic polymeric filaments. It is the most widely used 3D printing method, mainly because of the combination of low effort and high flexibility at low investment cost [14, 16].

The initial applications in reaction engineering were the preparation of laboratory equipment and reactors [17], followed by the preparation of catalyst supports and catalytic materials [18]. Based on FDM especially the processing of composite filaments poses a great challenge as they consist of the thermoplastic polymer as printable binder matrix and typically inorganic or hybrid solid particles as filler material. For example, Sorkski et al. used FDM to print an active catalyst for the photo degradation of Rhodamine 6G by incorporating TiO_2 nanoparticles into ABS filament [19]. Another recent example by Sun et al. is the catalysis of the Fenton oxidation of aromatic molecules by a catalytic

monolith made from a PLA filament containing an iron catalyst [20]. Zhu et al. manufactured hierarchical nanoporous gold monoliths [21]. They reported that the defined 3D structure improves mass transport and effective reaction rates in comparison to reference catalysts.

In recent years, the immobilization and shaping of nanoporous materials such as zeolites and metal-organic frameworks (MOFs) by additive manufacturing has attracted great attention, e.g., zeolites 5A and 13X have been printed as a paste with methylcellulose as binder [22]. This system is typically used for zeolite extrusion and hence, for the 3D printed monolith it was even possible to burn off the organic binder and obtain pure zeolite monoliths on the centimeter scale. A similar binder-free approach was shown for the MOF HKUST-1 that was printed as a gel, although, with low resolution only on the millimeter scale [23]. A somewhat different approach is based on the printing of a paste that consists of cellulose pulp fibers with surface-grown MOF particles [24]. Recently, also a covalent organic framework (COF) was printed from a pre-polymerized precursor gel with a subsequent posttreatment to achieve the full formation of the accessible framework material in a 3D monolithic structure [25]. These approaches can be considered rather specific for some individual type of materials as they can only be applied in case of a suitable precursor species that are printable. Hence, more common is the printing of composite monoliths. Several recent reports proved the concept to print various MOFs with typical thermoplastic

Sebastian Hock, Prof. Dr. Marcus Rose
rose@tc2.tu-darmstadt.de

Technische Universität Darmstadt, Ernst-Berl-Institut für Technische und Makromolekulare Chemie, Alarich-Weiss-Straße 8, 64287 Darmstadt, Germany.

polymers such as acrylonitrile butadiene styrene (ABS) and polylactic acid (PLA). [26–30]

The disadvantage of these composites in FDM printing is the relatively low loading of porous material, which is below 10 wt% in most cases. This is due to weak interactions between the MOF particles and the polymeric binders. Also, a thermoplastic polymer cannot be thermally posttreated, e.g., to achieve crosslinking or burn off the binder polymer. An increasing filler content often results in composites that are not printable anymore. On the other hand, the lower the filler content the higher the pore blocking from the binder polymer and thus, the functional inner surface of the porous materials is not well accessible anymore.

Based on MOFs and COFs in recent years porous organic polymers gained increased attention due to their intriguing properties for adsorption of organic compounds as well as their preparation routes that can be scaled up easily [31–33]. In our group, hyper-crosslinked polymers (HCP) are investigated for various applications such as liquid-phase adsorption [34, 35] and membrane nanofiltration [36]. Also, the synthesis routes have been improved in the past [37, 38]. The material is typically microporous with a small ratio of mesopores. Specific surface areas of up to $1842 \text{ m}^2 \text{ g}^{-1}$ can be achieved [37]. Due to the fact that HCP are purely organic materials the interactions with typical polymers are strong and, hence, a high loading degree of composite materials for 3D printing is expected.

The aim of this work is to use FDM 3D printing to design and manufacture different structured beds in the form of cylindrical monoliths with hierarchical porosity in that sense that a powdered microporous functional material is immobilized in a monolith with defined macroscopic transport pores in up to three dimensions. Accordingly, four differently structured monoliths are designed to perfectly fit a laboratory-scale tubular reactor. The most important hydrodynamic characteristics such as pressure drop and residence time distribution are determined experimentally. To functionalize the inner surface with typical microporous materials, in this case HCP, composite filaments are prepared for direct printing. By postprinting treatments a high accessibility of the inner surface is achieved. Thereby, it is proven that FDM is a suitable method to produce structured monoliths that contain microporous functional materials with the aim to enable their utilization in fixed-bed catalytic reactors and adsorbers.

2 Results and Discussion

2.1 Printing of Monoliths

Four monoliths with different geometries of the three-dimensional transport channels were designed with CAD to perfectly fit a tubular reactor with a length of 150.0 mm and a diameter of 29.5 mm (Fig. 1). The complexity of the structures increased from monolith I to IV. Monolith I consists of straight 1D pore channels comparable to conventional monoliths manufactured by extrusion. In contrast, monolith II is built up by an AB-type packing of filaments with orthogonal orientation that results in 1D axial pore channels with radial connections. Monolith III is built up similar to monolith II with the difference of an ABCD-type stacking, in which A and C as well as B and D, respectively, are shifted each by the diameter of 1 filament. Hence, no 1D straight pore channel exists but a 3D pore system with an increased tortuosity. In contrast, the geometry of IV consists of pore channels that form a diamondoid structure in which each channel connects to three other channels in a tetrahedral node. Based on the size, fibers and shape the monoliths were printed with a maximum deviation of $\pm 0.2 \text{ mm}$ over the full length. Also, all channels including the ones in structure IV are accessible and no obvious defects were observed. The monoliths fit the reactor precisely avoiding any dead volume or bypass flow during further testing of the hydrodynamic properties of the monoliths.

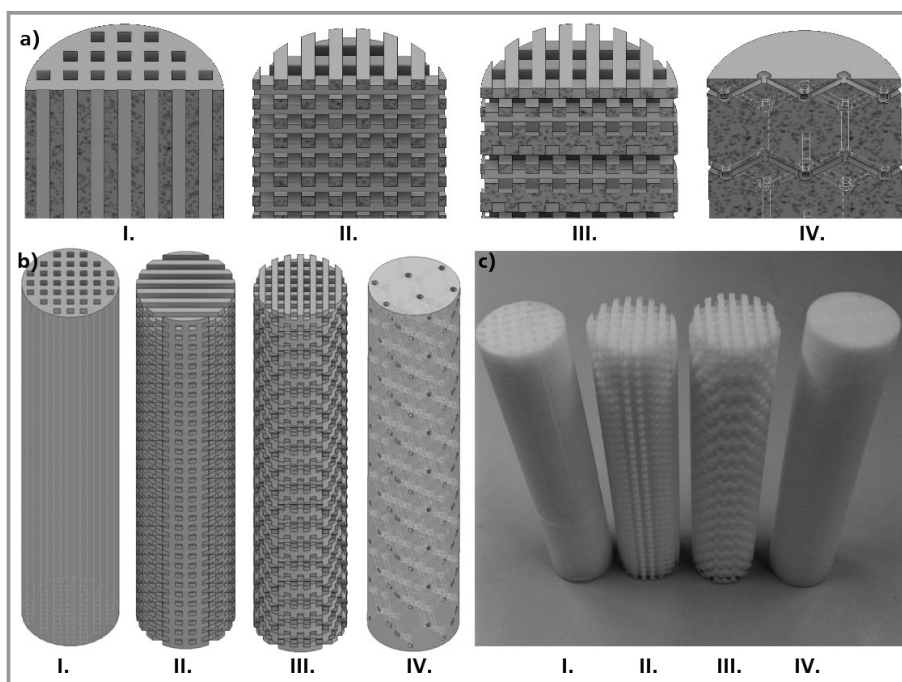


Figure 1. CAD designed monoliths: I with 1D pore channels; II with AB-type stacking and 1D pore channels with radial connections; III with ABCD-type stacking giving a higher tortuosity of the channels; and IV with pore channels that connect in tetrahedral nodes in a diamondoid structure.

2.2 Characterization of the Hydrodynamic Properties

The hydrodynamic properties, i.e., the pressure drop and the residence time distribution of the monoliths I–IV were experimentally determined using a tubular pressure reactor with a length of 150.0 mm and a diameter of 29.5 mm. The different setups for both parameters are shown in Fig. 2.

The pressure drop was measured with argon as inert gas in dependence of the volumetric flow rate in the range of 1–10 L min⁻¹. For every set volumetric flow rate the pressure drop was measured every second for 3 min under steady-state conditions to obtain the average value and the standard deviation. Monolith I and II show only a minor pressure drop with a similar dependency on the volumetric flow rate (Fig. 3). The structure of monolith III with a significantly higher tortuosity of the pore channels results in an approx. 50 % higher pressure drop compared to monolith II with radially connected 1D pore channels. In contrast, the more complex structure of monolith IV with a pore channel network of a diamondoid geometry causes a pressure drop that is significantly higher compared to monolith I–III and shows a linear increase with increasing volumetric flow rate.

The residence time distributions of monolith I–IV were experimentally determined by pulse experiments (Fig. 4). The liquid phase was water and as tracer a 5-wt % sucrose solution was used. The dependence of the mean residence time on the volumetric flow rate is shown in Fig. 5. Due to the 1D pore channels monolith I shows the narrowest residence time distribution compared to monoliths II–IV. Monolith II shows a somewhat similar distribution but with

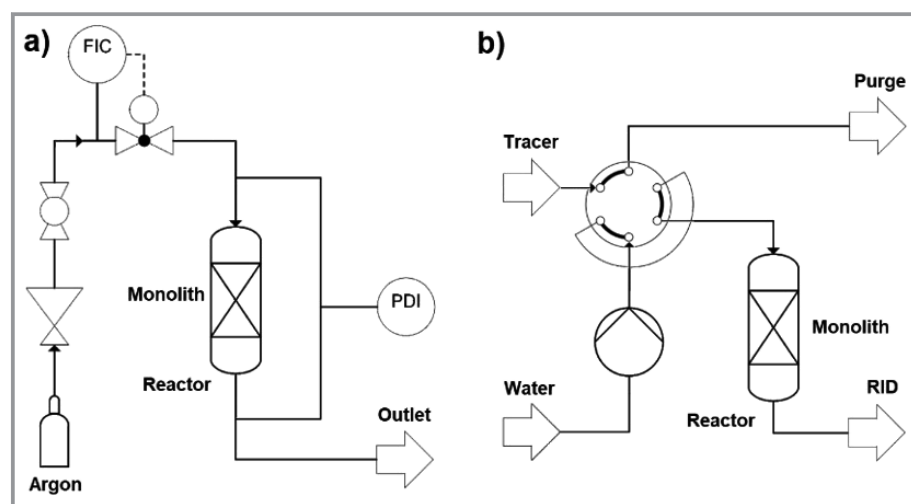


Figure 2. Experimental setups to determine the pressure drop (a) and the residence time distribution (b) of the tubular reactor containing the monoliths.

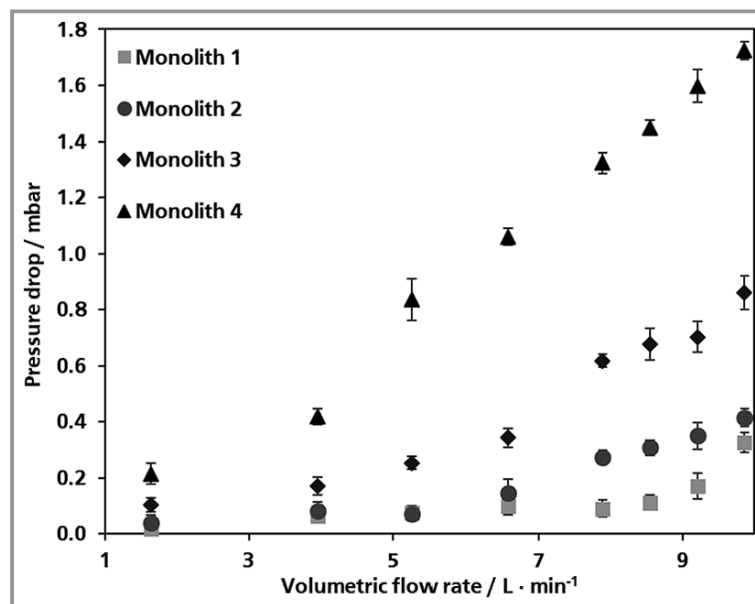


Figure 3. Pressure drop of monoliths I–IV in dependence on the volumetric flow rate of argon. Shown values represent the measured pressure difference at the reactor inlet and outlet.

an inferior slope and more pronounced tailing due to the radially connected pores that result in a more pronounced backmixing. When comparing the mean residence time of monolith I and II, an increasing difference with increasing volumetric flow rate is obvious. This can be ascribed to the stronger back mixing due to the connected pore channels in the cross section. In contrast, the structure of monolith III does not possess 1D pore channels and thus, prohibits a direct flow path. Hence, a higher mean residence time is observed. Similar to monolith II a strong tailing occurs due to the backmixing in the cross section.

The broadest residence time distribution is exhibited by monolith IV with its diamondoid pore channel structure connected by tetrahedral nodes. The very high mean residence time especially at a low volumetric flow rate (Fig. 5) can be explained by the presence of a relatively high amount of pore channels as dead volume directed towards the external surface of the monolith but without direct connection in the direction of flow. An artefact of this feature is the formation of a shoulder in the residence time distribution due to a fraction that passes the pore channels first followed by a large fraction with a higher residence time due to the relatively high number

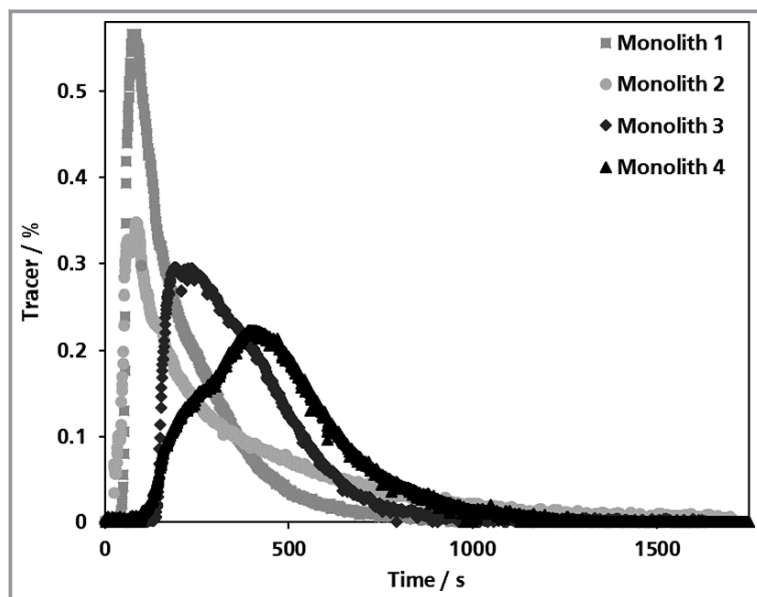


Figure 4. Residence time distribution of monoliths I–IV at a volumetric flow rate of 8 mL min^{-1} of water as the main fluid phase and 5-wt % sucrose solution as tracer.

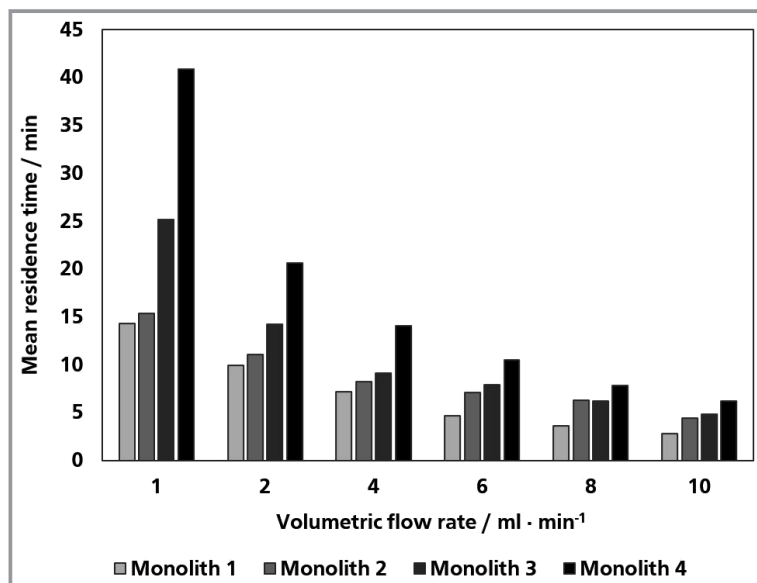


Figure 5. Comparison of the experimentally determined mean residence times of monoliths I–IV in dependence of the volumetric flow rate.

of dead-end pores. Overall, the significant influence of different pore channel structures on the hydrodynamic behavior of monolithic beds is proven.

2.3 Printing of HCP-Containing Filament

Nanoporous HCP proved to be an ideal model system for additive manufacturing by FDM with conventional thermo-

plastic polymers as composite filament because compared to typical inorganic or hybrid microporous materials such as zeolites or MOFs the HCP exhibit the best processability in combination with thermoplastic polymers since they consist solely of organic building blocks. Hence, to gain FDM-printable composite filament the ideal binder polymer and ratio of filler and matrix had to be determined. Therefore, various types of conventionally applied FDM polymers such as PS, PVA, PLA and ABS were combined with HCP particles in different ratios in order to determine the maximum amount of HCP as filler that can still be extruded into a flexible filament. The major issue is not only to achieve a high loading of HCP but rather to gain an accessible micropore network of the HCP. This was experimentally proven by measurement of the nitrogen physisorption and determination of the specific surface area.

Fig. 6a shows a selection of the prepared filaments and their correlating specific surface area. It was possible to produce filament with up to 40 wt % HCP. The highest specific surface areas were reached with a three-component filament, consisting of PVA, PS and HCP. The water solubility of PVA was used to gain additional accessibility of the HCP particles in the PS matrix by partial removal of the water-soluble PVA. With several washing steps the accessible specific surface area could be increased up to $383 \text{ m}^2 \text{ g}^{-1}$ (Fig. 6b), but there is a limit to the amount of PVA that can be dissolved. With repeated washing steps also an increasing loss of HCP occurs, resulting in a decrease of specific surface area. The ideal combination with PVA and HCP was obtained by the use of PS as binder polymer, which showed a better printability than the tested PLA and ABS filaments.

This optimized filament with the highest loading of HCP and the highest accessible specific surface area could also be printed into a 3D structure using a nozzle of 0.8 mm and adjustment of the printing temperature for each layer (Fig. 6c I.). Overall, 40 wt % HCP present the maximum quantity that is still printable. This high HCP content leads to a decrease of the printing quality and a significant drop of the overall stability of the monolith. The monolith with 40 wt % HCP is rather brittle in comparison to lower loadings. 30 wt % of HCP (Fig. 6c II.) can be achieved without a loss in mechanical stability and proves that printing of filament containing 30 wt % HCP is possible in the same quality as filler-free filament (Fig. 6c III.). The printed monolith consisting of 40 wt % HCP, 40 wt % PVA and 20 wt % PS exhibits a specific surface area of $160 \text{ m}^2 \text{ g}^{-1}$, which could be increased to

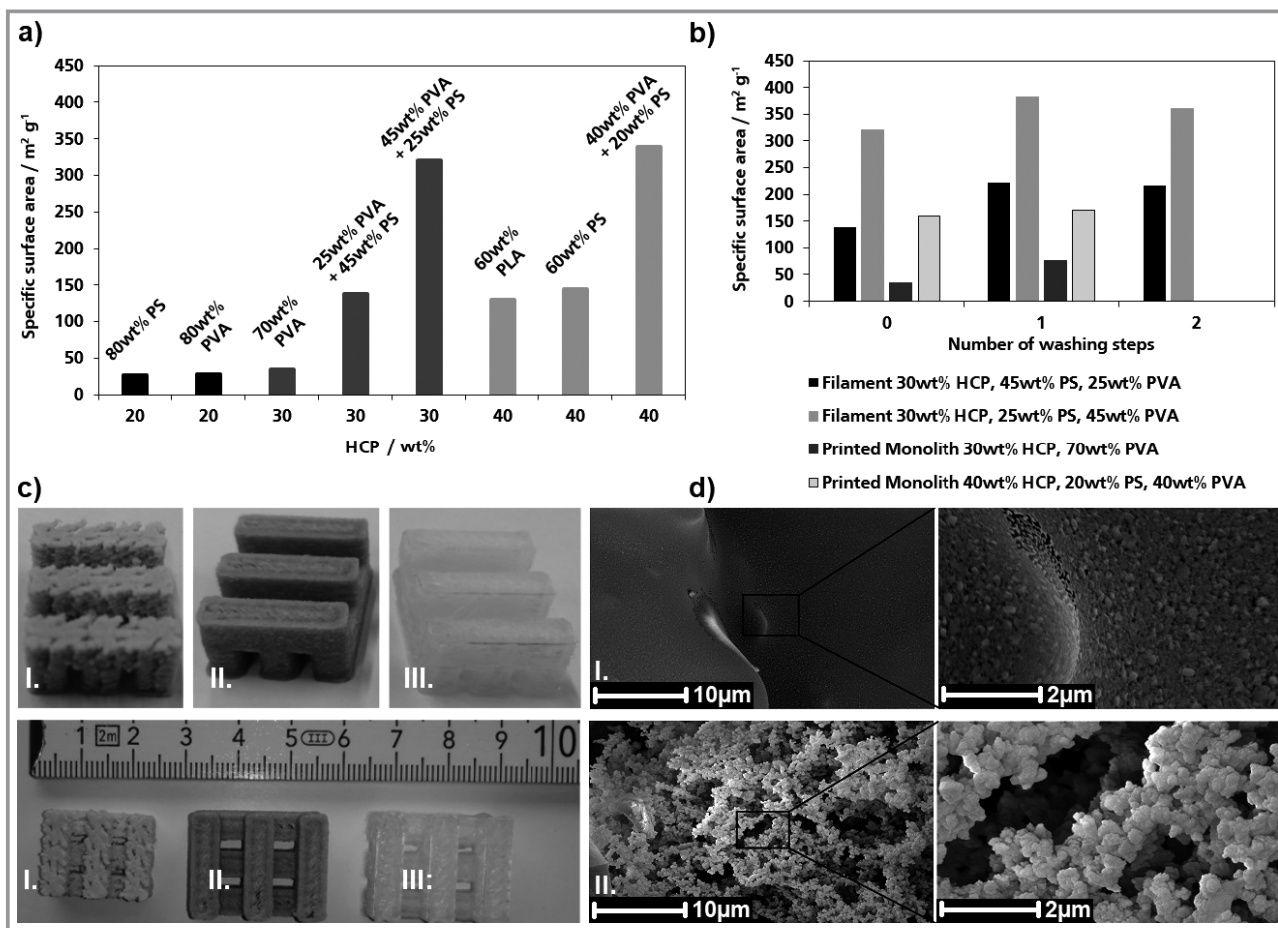


Figure 6. a) Composition of the different prepared filaments and their specific surface area; b) change of the specific surface area of the filaments and monoliths with soluble PVA in regard to the number of washing steps; c) printed monoliths: I. 40 wt % HCP, 40 wt % PVA, 20 wt % PS; II. 30 wt % HCP, 70 wt % PVA; III. pure PVA; d) I. SEM images of the surface of monolith I; d) II. SEM images of the edge after breaking of monolith I after washing.

171 m²g⁻¹ by partially dissolving the PVA. The maximum specific surface area that can be achieved decreases with every melt extrusion step, in this case also by the final FDM printing step. Hence, too strong interactions of filler and matrix polymer are probably counterproductive as the wetting of the inner pore surface during melting increases and partial pore blocking increases.

The obtained HCP-containing monoliths were additionally investigated by SEM imaging of the surface (Fig. 6d). HCP in PVA/PS as well as HCP in PVA both show a homogenous distribution of the HCP particles on the surface (Fig. 6d I) as well as on a breaking edge inside the monolith (Fig. 6d II). Still, due to the organic nature of the HCP and the binder polymer from SEM the pore blocking of the microporous HCP particles is not visible. Hence, only by physisorption measurements conclusions about the accessibility can be drawn.

3 Conclusion

FDM-based 3D printing of abundant and affordable thermoplastic polymers is applied to print structurally well-resolved monoliths as fixed beds. Four monoliths are designed to precisely fit a laboratory scale tubular reactor with a diameter of 29.5 mm and a length of 150.0 mm. The hydrodynamic properties pressure drop and residence time distribution are experimentally investigated. The tailor-made structures with differences in pore channel geometries exhibit significantly different characteristics. Hence, the suitability of 3D printing or additive manufacturing in general for reaction engineering purposes concerning reactors or other units that require structured packings of any kind is proven. Furthermore, the FDM 3D printing of composite filaments of a nanoporous polymer and thermoplastic binder polymers proves that loadings of the nanoporous solid material of up to 40 wt % can be extruded into 3 mm filaments and precisely printed into 3D structures. The issue of pore blocking by the melt extrusion process can be

overcome by applying polymer mixture with PVA as a water-soluble component. Specific surface areas of up to $171 \text{ m}^2 \text{ g}^{-1}$ are obtained for the HCP-containing monoliths. In summary, FDM is a versatile and flexible tool to produce monolithic structures with tailor-made transport pore channels. By printing of composite filaments functional porous materials can be incorporated into the pore walls of the macropore structure. However, depending on the type of porous filler material an individual optimization regarding the loading and pore blocking is always necessary.

4 Experimental Section

4.1 Materials

4,4'-Bis(chloromethyl)1-1'-biphenyl (BCMBP, 95 %) and 1,2-dichloroethane (DCE, 99%) were purchased from Sigma Aldrich. Ethanol (EtOH, 96 %), granulated polyvinyl acetate (PVA 87–90 % hydrolyzed and granulated polystyrene (PS, 99%) were obtained from Carl Roth. Trifluoromethanesulfonic acid ($\text{CF}_3\text{SO}_3\text{H}$, 99%) was purchased from Fluorochem. PLA pellets were obtained from 3D-PrintShop. All chemicals were used as received.

4.2 Printing of Monoliths

The monoliths were designed with the software Autodesk Inventor[®] for a precise fit into a tubular reactor with a diameter of 29.5 mm and a length of 150.0 mm. The .stl files were converted into .gcode with the software Renkforce Repetier[®] host and printed with a Renkforce RF2000 3D printer using PS filament (3D Printshop, Berlin). For the required adhesion of the HCP-containing monoliths, a heat bed temperature of 120°C in combination with an adhesive foil was applied. The extrusion temperature for the first layer was 230°C . The temperature of the following layers was varied between 205°C and 220°C depending on the HCP content. With rising HCP content, a higher printing temperature is required.

4.3 Measurements of Pressure Drop and Residence Time

The 3D-printed monoliths were placed in a tubular reactor. The measurement of the pressure drop was carried out with a differential pressure sensor from Aplisens, type APRE-2000, using volume flows of $1\text{--}10 \text{ L min}^{-1}$ of argon. The measurement of the residence time was achieved using a 6-port valve with a sample loop and an online refractive index detector (RID) for detection. Water was used as the main phase and 5-wt % sucrose solution as tracer.

4.4 Synthesis of HCP

In this work the applied HCP was synthesized according to Rose et al. [37]. BCMBP (40.0 mmol) was dissolved in 1,2-dichloroethane (DCE, 100 mL) and trifluoromethanesulfonic acid ($\text{CF}_3\text{SO}_3\text{H}$, 60.5 mmol) was added dropwise. The solution was stirred for 1 h. The product was filtered and washed using ethanol and water, then dried under vacuum. [37]

4.5 Preparation and Printing of Microporous Filament

For the preparation of the composite filaments with HCP as filler with intrinsic microporosity ball-milled polymer (PLA, PVA, PS or a mixture) were combined with HCP in defined ratios. The physical mixture was then extruded into a filament with a diameter of 3 mm suitable for FDM printing using a Noztek Pro[®] at 200°C .

4.6 Characterization

Nitrogen physisorption measurements were carried out with a Quadrasorb EVO from Quantachrome Instruments. The pre-dried samples were degassed under vacuum at 100°C for 20 h. The BET specific surface area was determined in the relative pressure region $p/p_0 = 0.05\text{--}0.25$.

SEM images were taken on a HREM XL 30 FEG from Philips with 10 keV and detection of the secondary electrons. For a sufficient conductivity the samples were sputtered with gold with 30 mA für 120 s.

We gratefully acknowledge financial support by the Federal Ministry of Education and Research (BMBF), Grant No. 031B0678B.

Abbreviations

ABS	acrylonitrile butadiene styrene copolymer
BCMBP	4,4'-bis(chloromethyl)1-1'-biphenyl
COF	covalent organic framework
DCE	1,2-dichloroethane
FDM	fused deposition modeling
HCP	hyper-crosslinked polymer
MOF	metal-organic framework
PLA	polylactic acid
PS	polystyrene
PVA	polyvinylalcohol
RID	refractive index detector

References

- [1] C. Fee, S. Nawada, S. Dimartino, *J. Chromatogr. A* **2014**, *1333*, 18–24.
- [2] A. Daneyko, A. Höltzel, S. Khirevich, U. Tallarek, *Anal. Chem.* **2011**, *83*, 3903–3910.
- [3] S. Khirevich, A. Daneyko, A. Höltzel, A. Seidel-Morgenstern, U. Tallarek, *J. Chromatogr. A* **2010**, *1217*, 4713–4722.
- [4] A. Daneyko, S. Khirevich, A. Höltzel, A. Seidel-Morgenstern, U. Tallarek, *J. Chromatogr. A* **2011**, *1218*, 8231–8248.
- [5] M. Klumpp, A. Inayat, J. Schwerdtfeger, C. Körner, R. F. Singer, H. Freund, W. Schwieger, *Chem. Eng. J.* **2014**, *242*, 364–378.
- [6] S. Didierjean, H. P. A. Souto, R. Delannay, C. Moyne, *Chem. Eng. Sci.* **1997**, *52*, 1861–1874.
- [7] H. Eghbali, V. Verdoold, L. Vankeerberghen, H. Gardeniers, G. Desmet, *Anal. Chem.* **2008**, *81*, 705–715.
- [8] N. V. Lavrik, L. C. Taylor, M. J. Sepaniak, *Lab Chip* **2010**, *10*, 1086–1094.
- [9] A. Ambrosi, M. Pumera, *Chem. Soc. Rev.* **2016**, *45*, 2740–2755.
- [10] M. Guvendiren, J. Molde, R. M. Soares, J. Kohn, *ACS Biomater. Sci. Eng.* **2016**, *2*, 1679–1693.
- [11] P. J. Kitson, M. D. Symes, V. Dragone, L. Cronin, *Chem. Sci.* **2013**, *4*, 3099–3103.
- [12] B. Utela, D. Storti, R. Anderson, M. Ganter, *J. Manuf. Process.* **2008**, *10*, 96–104.
- [13] C. Minas, D. Carnelli, E. Tervoort, A. R. Studart, *Adv. Mater.* **2016**, *28*, 9993–9999.
- [14] X. Zhou, C.-j. Liu, *Adv. Funct. Mater.* **2017**, *27*, 1701134.
- [15] C. Parra-Cabrera, C. Achille, S. Kuhn, R. Ameloot, *Chem. Soc. Rev.* **2018**, *47*, 209–230.
- [16] P. Dudek, *Arch. Metall. Mater.* **2013**, *58*, 1415–1418.
- [17] J. A. Lewis, *Adv. Funct. Mater.* **2006**, *16*, 2193–2204.
- [18] T. Tabassum, M. Iloska, D. Scureb, N. Taira, C. Jin, V. Zaitsev, F. Afshar, T. Kim, *J. Chem. Ed.* **2018**, *95*, 783–790.
- [19] M. R. Skorski, J. M. Esenther, Z. Ahmed, A. E. Miller, M. R. Hartings, *Sci. Technol. Adv. Mater.* **2016**, *17*, 89–97.
- [20] X. Sun, Y. Yan, L. Zhang, G. Ma, Y. Liu, Y. Yu, Q. An, S. Tao, *Adv. Mater. Interfaces* **2018**, *5*, 1701626.
- [21] C. Zhu, Z. Qi, V. A. Beck, M. Luneau, J. Lattimer, W. Chen, M. A. Worsley, J. Ye, E. B. Duoss, C. M. Spadaccini, C. M. Friend, J. Biener, *Sci. Adv.* **2018**, *4*, eaas9459.
- [22] H. Thakkar, S. Eastman, A. Hajari, A. A. Rownaghi, J. C. Knox, F. Rezaei, *ACS Appl. Mater. Interfaces* **2016**, *8*, 27753–27761.
- [23] G. J. H. Lim, Y. Wu, B. B. Shah, J. J. Koh, C. K. Liu, D. Zhao, A. K. Cheetham, J. Wang, J. Ding, *ACS Mater. Lett.* **2019**, *1*, 147–153.
- [24] S. Sultan, H. N. Abdelhamid, X. Zou, A. P. Mathew, *Adv. Funct. Mater.* **2019**, *29*, 1805372.
- [25] M. Zhang, L. Li, Q. Lin, M. Tang, Y. Wu, C. Ke, *J. Am. Chem. Soc.* **2019**, *141*, 5154–5158.
- [26] Z. Wang, J. Wang, M. Li, K. Sun, C.-j. Liu, *Sci. Rep.* **2014**, *4*, 5939.
- [27] M. C. Kreider, M. Sefa, J. A. Fedchak, J. Scherschligt, M. Bible, B. Natarajan, N. N. Klimov, A. E. Miller, Z. Ahmed, M. R. Hartings, *Polym. Adv. Tech.* **2018**, *29*, 867–873.
- [28] K. A. Evans, Z. C. Kennedy, B. W. Arey, J. F. Christ, H. T. Schaeff, S. K. Nune, R. L. Erikson, *ACS Appl. Mater. Interfaces* **2018**, *10*, 15112–15121.
- [29] O. Halevi, J. M. R. Tan, P. S. Lee, S. Magdassi, *Adv. Sustainable Sys.* **2018**, *2*, 1700150.
- [30] M. Bible, M. Sefa, J. A. Fedchak, J. Scherschligt, B. Natarajan, Z. Ahmed, M. R. Hartings, *3D Print. Addit. Manuf.* **2018**, *5*, 63–72.
- [31] N. Chaoui, M. Trunk, R. Dawson, J. Schmidt, A. Thomas, *Chem. Soc. Rev.* **2017**, *46*, 3302–3321.
- [32] L. Tan, B. Tan, *Chem. Soc. Rev.* **2017**, *46*, 3322–3356.
- [33] S. Xu, Y. Luo, B. Tan, *Macromol. Rapid Commun.* **2013**, *34*, 471–484.
- [34] K. Schute, C. Detoni, A. Kann, O. Jung, R. Palkovits, M. Rose, *ACS Sustainable Chem. Eng.* **2016**, *4*, 5921–5928.
- [35] L. Rübenach, J. Lins, E. Koh, M. Rose, *ChemSusChem* **2019**, *12*, 3627–3634.
- [36] K. Schute, F. Jansen, M. Rose, *ChemNanoMat* **2018**, *4*, 562–567.
- [37] K. Schute, M. Rose, *ChemSusChem* **2015**, *8*, 3419–3423.
- [38] S. Grätz, S. Zink, H. Krafczyk, M. Rose, L. Borchardt, *Beilstein J. Org. Chem.* **2019**, *15*, 1154–1161.